Progress in K-DEMO Heating/Current Drive and Tokamak Configuration Development*

G. H. Neilson[1], D. Mikkelsen[1], C. Kessel[1], T. Brown[1], P. Titus[1], H. Zhang[1], K. Im[2], J. S. Park[2,] S. Kwon[2]

[1] Princeton Plasma Physics Laboratory, Princeton, NJ 08543 U.S.A.
[2] National Fusion Research Institute, Daejeon 34133, the Republic of Korea

e-mail contact of main author: hneilson@pppl.gov

Abstract. Analyses of the plasma heating and current drive configuration and aspects of the tokamak configuration for K-DEMO are reported. A combination of heating and current drive technologies, i.e., lower hybrid waves (LH), neutral beams (NB), electron cyclotron waves (EC), and ion cyclotron conventional fast waves (IC) is considered for satisfying multiple requirements, including steady state current drive. Parameter scan calculations for each of the four technologies have quantified the dependence of key performance metrics, such as driven current per watt and radial profile, on design variables. Tokamak configuration studies have investigated requirements on the in-vessel systems for maintainability, access for piping services, and structural support against magnetic forces. The blanket-shield system is segmented into a small number (48) of large modules, supported in part by a segmented semi-permanent inboard shell. Structural analysis has addressed stresses due to eddy currents resulting from a vertical-displacement event disruption, static forces due to the magnetic materials in the blanket structures, and thermal stresses.

1. Introduction

The K-DEMO [1,2,] machine is being studied by S. Korea's National Fusion Research Institute as a possible next-step fusion nuclear facility with a mission to test fusion nuclear components in Phase I and, after upgrades, to produce ≥2,200 MW of fusion power and ≥400 MW of electricity in a Phase II. The study is based on a steady state tokamak with toroidal magnetic field B_T = 7.4 T on axis, major radius R = 6.8 m, minor radius a = 2.1 m. Parameters for a representative operating point are plasma current I_P = 12.3 MA, line-averaged density $\bar{n}$ =1.1×10^{20} m^{-3}, central plasma temperature T(0) = 40 keV, and Z_{eff}=1.5.

2. Plasma Heating and Current Drive Configuration

The K-DEMO facility will require systems to drive the plasma into the burn state and then sustain it, supplementing the bootstrap current in providing over 12 MA of fully non-inductively driven plasma current in steady state. A preliminary time-dependent simulation [1] of a scenario typical of Phase I, from start-up to a sustained burn at Pfus = 1,500 MW, used 120 MW of auxiliary heating to supplement 310 MW of alpha-particle heating and to drive 3.9 MA of plasma current, supplementing 8.4 MA of bootstrap current. Phase I conditions were chosen because they have lower beta and lower contribution from bootstrap current, so they are conservative for sizing the external heating and current drive power requirements. A combination of heating and current drive technologies, i.e., lower hybrid waves (LH), neutral beams (NB), electron cyclotron waves (EC), and ion cyclotron conventional fast waves (IC) is considered for satisfying multiple requirements, including steady state current drive. To provide the information needed for optimization, scans of key system variables, e.g. frequency, phasing, location, or orientation, were performed.

2.1. Lower hybrid waves.

Lower hybrid can provide current off-axis, and at the high toroidal field and low density of K-DEMO, the accessibility of these waves is very good. The minimum accessibility condition is $n_{||} > 1.4$, but the current drive is maximized by avoiding mode-conversion to the fast wave with $n_{||} \sim 1.7$-2.0, depending on the poloidal location of the launcher. The current drive can

* Research supported by the National Fusion Research Institute, Daejeon, the Republic of Korea, under a research agreement with Princeton University, and by the U.S. Department of Energy under Contract No. DE-AC02-09CH11466 with Princeton University.

reach inward to r/a~0.65, with a broad profile outward to the edge. We chose a frequency of 5 GHz to avoid alpha particle absorption, and this is low enough to avoid excessively small waveguide dimensions. The ITER passive-active multi-junction (PAM) launcher concept [3, 4] is used here, which has co-I_p and cntr-I_p power fractions of ~ 70% and ~ 30%, respectively and has been demonstrated to have a power density 20 MW/m^2

The Lower Hybrid Simulation Code (LSC) [5] is used to provide a 1D ($v_{||}$) Fokker-Planck ray tracing analysis. The $n_{||}$ and launching angle on the outboard side were scanned to find the optimum for current drive. The forward power lobe is scanned from $n_{||}$ = 1.85-2.5 and is assumed to carry 87%. The power split between forward and backward lobes is used to provide a correction factor of 1.6 to the LSC prediction, and is determined by comparison with more accurate GENRAY/CQL3D 2D Fokker-Planck calculations [6, 7, 8].

Figure 1 shows the lower hybrid analysis results, showing the total driven current as a function of the forward $n_{||}$ launched, with curves representing outboard launching locations from -60 to 60^o. The trend of decreasing current drive efficiency at the lowest $n_{||}$ corresponds to increasing conversion of the slow waves to fast waves, which propagate back to the separatrix and reflect into the plasma with $n_{||}$ upshifts and subsequent damping close to the separatrix (of the fast waves). The trend of decreasing current drive efficiency at larger $n_{||}$ is due to full absorption at progressively shallower penetration depths, and the associated lower temperatures limit the attainable driven current. The highest current drive efficiency found in the K DEMO study is 0.22 A/W-m^2 (= n_{20}RI/P). Launching from an off-midplane elevation provides the highest current drive per watt, and yields deeper penetration of the LH waves as well as broader current distributions. Since the launching structure displaces some breeding blanket volume it is advantageous for tritium breeding to move the launcher away the midplane where the neutron flux peaks.

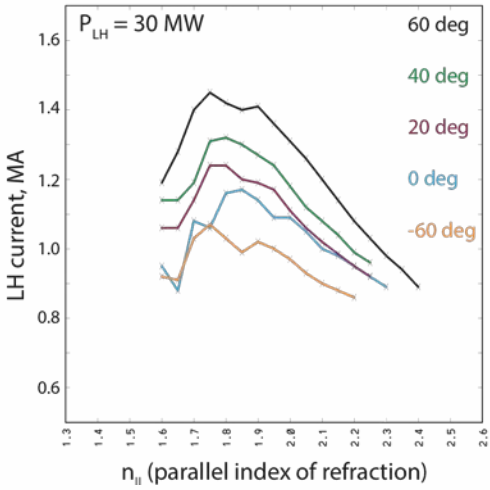

Figure 1. LH total driven current as a function of the forward launch $n_{||}$ and launch location above /below the outboard midplane.

2.2. Neutral beam injection

A negative-ion neutral beam (NB) with particle energy ~1 MeV, like that proposed for ITER, could provide customized profiles of heating and current drive with high efficiency in the K-DEMO plasma with a density ~1.0×10^{20} m^{-3}, and central temperatures of ~40 keV. The ITER NB characteristics [9] have been adopted for the survey calculations. The beam arrangement and the size of the opening through the coils and blanket modules takes into account several competing considerations– minimizing the impact on tritium breeding and neutron streaming, minimizing ripple trapping and shinethrough, and maximizing current drive efficiency. The resulting compromise leads to choosing a tangency radius inside the plasma but not far from the inside wall, R_{tang} = 4.95 m in the case of K-DEMO. Providing neutral beam current drive at intermediate radii, 0.2<r/a<0.65, i.e., between the locations of ICRF fast-wave and lower-hybrid wave current drive, is most conveniently achieved with the horizontally-oriented neutral beams elevated off the midplane.

The NUBEAM [10] Monte Carlo orbit following package was used to calculate the NB deposition and collisional slowing down in the plasma. Shown in Figure 2 are a series of current density profiles for a range of beam axis displacements from 0.15 to 2.2 m off the

midplane. The total current driven by 50 MW of NB at each elevation Z is listed in the legend. The time-dependent simulation in ref. [1] assumed that 2 MA could be driven by the 50 MW of NB included in that simulation, and these detailed calculations confirm that the assumed efficiency can be met. Current profile control simulations of two combinations of beamlines at three different off-midplane elevations, provided in Figure 3, show that NB current drive can fill in the "gap" at intermediate radii.

The results in Figure 2 correspond to current drive efficiencies of $n_{e,20}R_oI_{cd}/P_{NB}$ = 0.3-0.4 A/W-m^2 or I_{cd}/P_{NB} = 0.04-0.06 A/W, with the higher efficiencies at larger r/a, where the density is lower. This is attractive for driving large amounts of current, and the radial location is not restricted so neutral beams can fill the current drive gap between the central deposition of ICRF fast waves at r/a < 0.25 and lower hybrid wave deposition at r/a > 0.65.

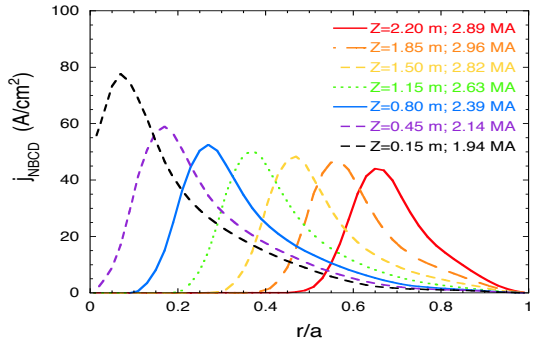

Figure 2. Beam-driven current density profiles for a range of beam axis displacements below the midplane from 0.15 to 2.2 m. The total current driven by 50 MW of NB at each Z is listed in the legend.

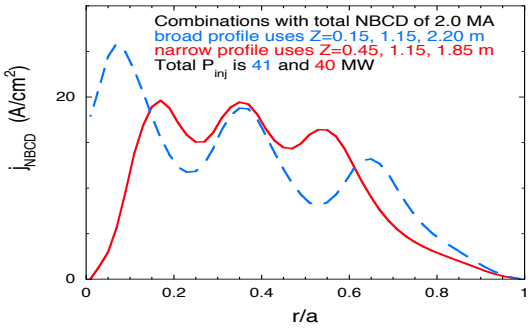

Figure 3. Beam-driven current density profiles from combinations of three orientations, where the power of the larger |Z| beams has been reduced to lower the total driven current to 2 MA.

2.3. Electron cyclotron waves.

Electron cyclotron waves current drive is examined as an alternative to neutral beams for providing current drive in the intermediate region of the plasma, with 0.2 < r/a < 0.6. The optimal conditions for heating and current drive via electron cyclotron waves are more complex than for other techniques because the damping in a hot plasma is enabled by a Doppler-shifted resonance between the waves and a small portion of the electron population [11]. The wave frequency, ω, and path through the plasma that defines the variation of $n_{||}$, as well as the electron temperature all play critical roles. We have focused on current drive in the conditions of the full power plasma burn since this is the primary need for the ECCD system. The parameters and profile shapes are taken from the time-dependent simulation in ref. [1]. The fundamental O-mode is launched from a location just outside the plasma on the low-field side. The condition for the waves to avoid significant refraction satisfied with the frequencies studied here. The GENRAY ray-tracing code [6,7] was used to calculate both ray propagation and current drive by electron cyclotron waves. Details of the physics models and assumptions for absorption, current drive, and wave-particle interactions are described elsewhere [12, 13, 14]

For a fixed electron temperature profile, finding the optimal parameters of the ECCD components requires a four dimensional parameter scan, varying the wave frequency, launcher position, and both the poloidal and toroidal steering angles defining the direction of the launched waves. With the high temperature of the burn phase, $T_e(0) \sim 40$ keV, it is critical to minimize second harmonic absorption [15] so that power is not absorbed by a resonance with low current drive efficiency. The frequency is varied from 190 to 300 GHz, while the launcher position is varied from the outer mid-plane to near the top of plasma. Reduced second harmonic losses have been reported for off-midplane launch [16, 17] and "top" launch

[18], so those configurations are of interest. Although the range of poloidal and toroidal launch angles was tailored to each launcher position, the occasionally strong dependence on launch angles required close spacing (1 degree), so the total number of calculations at each frequency/launcher position pair ranged from ~500 to ~1700.

2.3.1. Midplane launch

Figure 4 provides an overview of the results for *midplane* launchers, placed at R=8.96 m. The highest current drive efficiency is obtained at the highest frequencies, but only for current driven outside r/a ≈ 0.5. Absorption near the magnetic axis at these frequencies requires higher $n_{||}$, and this leads to strong second harmonic absorption at mid-radius, leaving little or no power to drive current near the axis. Current drive at the fundamental resonance is possible with the higher frequencies for targeted r/a ≥ 0.5 region. Second harmonic absorption is not a significant problem for frequencies up to ~210 GHz; all locations are accessible with similar efficiency, but it is uniformly low: only 15-25 A/kW. The $2\Omega_{ce}$ absorption is quite strongly dependent on current drive location as shown in Figure 5, with this loss channel growing rapidly as r/a diminishes or frequency rises.

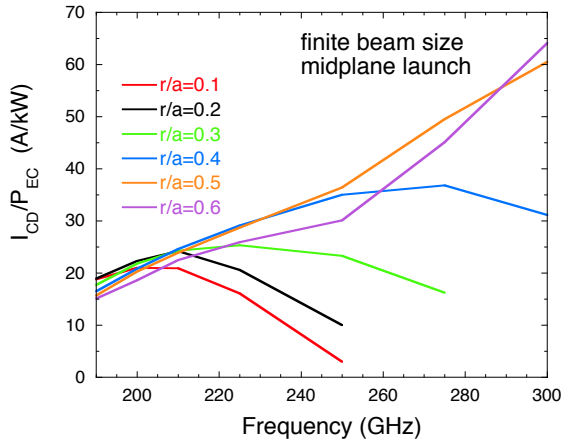

Figure 4. Electron cyclotron wave current drive efficiency vs. frequency, grouped by the average r/a of the driven current.

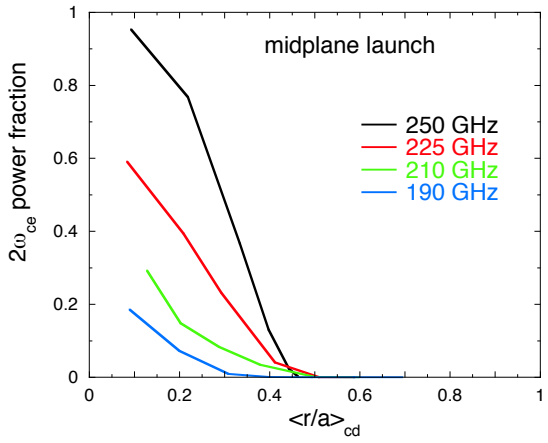

Figure 5. Power fraction absorbed by Doppler matching at the second harmonic vs. the average r/a of the driven current.

2.3.2. Off-midplane launch

Launching from an off-midplane elevation and smaller R serves to reduce second harmonic absorption by avoiding the outboard part of the plasma where the local second harmonic is closer to the wave's frequency and resonance is more easily achieved. By this means, access to the full range of r/a with reasonable current drive efficiency is still achievable at 225 GHz, although $2\Omega_{ce}$ absorption continues to severely reduce the current drive efficiency for small r/a at higher frequencies. Most of the benefit of reduced second harmonic absorption is obtainable without approaching so-called "top launch," where access is much more difficult. In spite of reduced second harmonic absorption, launcher positions off the midplane do not actually provide much improvement in current drive efficiency when finite-size beams of EC radiation are modeled (Figure 6).

In summary, the highest EC current drive efficiency is achieved with 275-300 GHz, but is limited to r/a ≥ 0.5. High efficiency at r/a ~ 0.4 is possible with 250 GHz, but smaller radii require lower frequencies and correspondingly lower efficiencies. The frequency range 190-210 GHz, launched from the outer midplane provides the greatest flexibility in current drive location, reaching normalized minor radius of 0.1- 0.6, but with current drive efficiency of only 15-25 A/kW (varying with frequency, not r/a). Although providing bulk plasma current with EC is impractical with these low efficiencies, its flexibility in deposition can be useful for controlling the safety factor profile and stabilizing neoclassical tearing modes and sawteeth [16, 17]. In analyzing local-control applications such as these, a finite size EC beam model should be used, since the single-ray approximation can underestimate the width of the driven current profile.

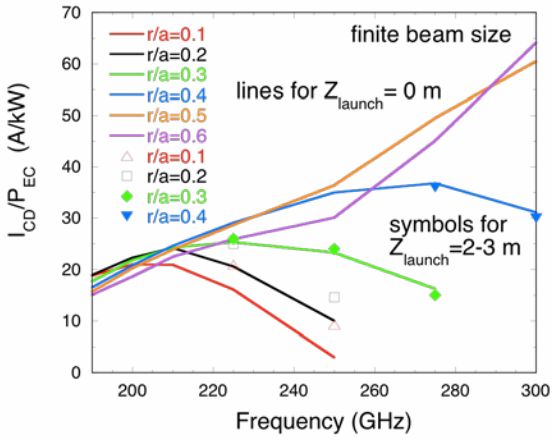

Figure 6. Electron cyclotron wave current drive efficiency vs. frequency. grouped by the average r/a of the driven current. Lines denote midplane launchers, isolated symbols represent off-midplane launchers.

2.4. Ion cyclotron fast waves.

Electromagnetic waves in the ion cyclotron range of frequencies, or ICRF, can be used to heat and to drive current near the magnetic axis with a relatively narrow distribution, typically for r/a ≤ 0.3. Optimizing the ICRF system parameters for current drive involves maximizing both the wave damping on electrons and the asymmetry in their velocity space distribution that is responsible for generating a net current, while avoiding the strong ion resonances that damp the waves before they can reach the hot electrons near the magnetic axis.

The TORIC full-wave code [19] is used to calculate ICRF fast-wave current drive and heating in the frequency range 50-110 MHz, with antenna characteristics based on the ITER multi-strap launcher design [20], which has a maximum power density through the first wall of 10 MW/m^2. With the antenna placed at the outboard midplane of K-DEMO, the toroidal mode number is 30. The driven current profiles for frequencies in the most effective range are provided in Figure 7. At lower and higher frequencies, wave power absorption at ion resonances reduces the power coupled to the electrons and hence the current drive. Fast-ion acceleration (mainly of alpha particles) can best be minimized in the range 74-80 MHz, where the current drive efficiency, 60-70 A/kW, is near its maximum. This conclusion is robust against changes in the toroidal wave number (varied from 23 to 37 in additional full frequency scans).

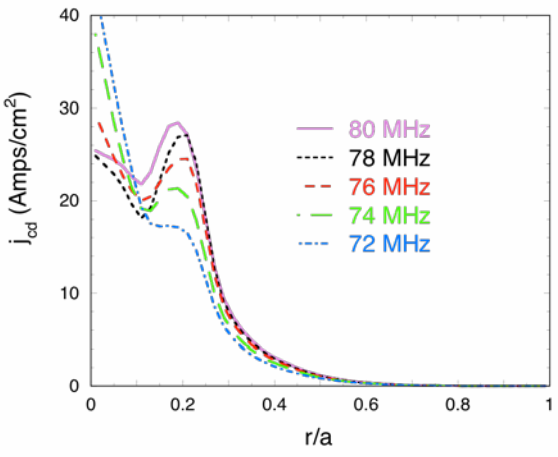

Figure 7. Ion cyclotron heating current drive profiles vs. minor radius in the most favorable frequency range.

3. Tokamak Configuration

3.1. Design

The overall machine configuration and structural analysis of the magnets were reported in ref. [1]. Recent work has focussed on the in-vessel systems, particularly issues of maintainability, piping services, and structural support against magnetic forces. The blanket/shield system (Figure 8) is segmented into 48 "banana" shaped sub-modules: 16 inboard and 16 outboard under each TF coil and 16 outboard located between TF coils. A 16-segment, semi-permanent shell supports the inboard modules. Water-cooled ceramic breeder blanket modules have been designed and subjected to extensive nuclear and thermal evaluations by NFRI [21]. The main structural loads on these components are expected to arise from disruption-induced eddy currents, from direct magnetic forces on the magnetic materials, especially RAFM steel, in the components, and from thermal stresses.

The structural concept considered here includes a semi-permanent inboard shield that also serves as support for the blanket modules, as well as inboard and outboard support shells. The inboard blanket support structure and the outboard blanket structure are toroidally electrically continuous and are structurally connected. The inboard modules are keyed into the toroidally continuous support structure which reacts disruption loads from the blankets and from its own internal eddy currents and static magnetic loads. The support shells serve as nuclear and electromagnetic shields for the vessel. This arrangement is a part of a vertical maintenance concept, that removes the inboard blanket module components with a radial and vertical traverse and leaves much of the massive shielding and support structure in place.

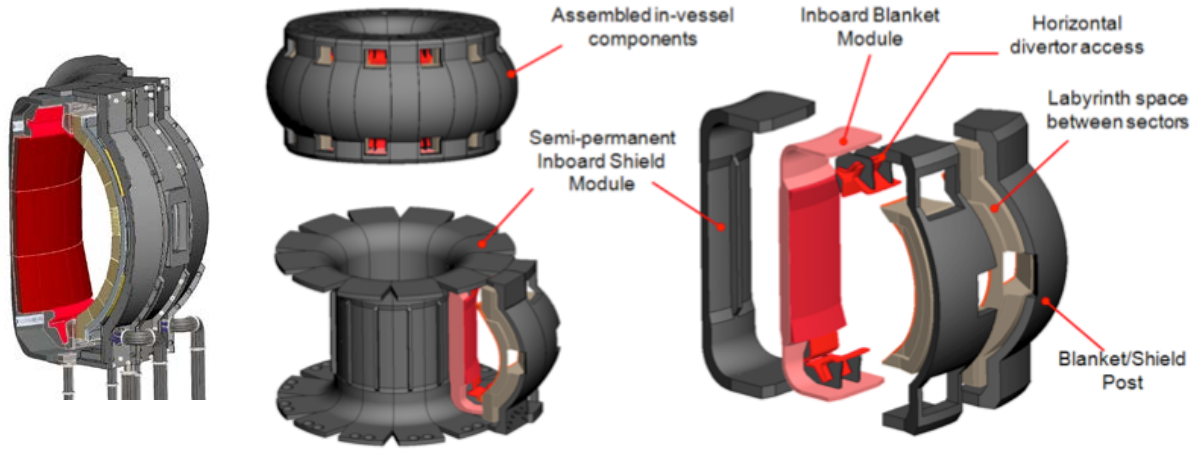

Figure 8. K-DEMO in-vessel systems, coolant feeds, and exploded details.

3.2. Stresses due to Disruption-Induced Eddy Currents

An ANSYS simulation of a vertical-displacement event (VDE) is used to generate local values of magnetic field and its time derivative on components in a 3D structual model and to calculate the resulting eddy currents and forces. The VDE drift and current quench times for these preconceptual scoping analyses, 0.8 s and 36 ms respectively, are based on ITER disruption parameters. An approximate, but representative model of the blanket is used. Significant nuclear effects on materials have not been considered.

To facilitate loading of a blanket module with disruption eddy current loads, a procedure which imposes a vector potential boundary condition based on the local fields and their time derivatives is used. This is usually a conservative approach because it can underestimate the inductive flux exclusion by the conducting structures. An outboard blanket module near the divertor is analyzed; at this locations the fields and their time derivatives are expected to produce the most significant loading. The disruption eddy current stresses are relatively modest (180 MPa) and peak around the attachment points (Figure 9).

3.3. Effects of Ferromagnetic Structure Material

The model used to evaluate the effect of using ferromagnetic materials in the structure of the blankets employs the edge flux formulation in ANSYS Solid236 elements. A simplified version of a K-DEMO blanket module composed partially of reduced activation ferritic/-martensitic (RAFM) steel is used; typical of the blankets considered at PPPL is a RAFM fraction of ~20%. In a study varying the fraction of RAFM it is found that static forces and moments scale fairly linearly with RAFM fraction.

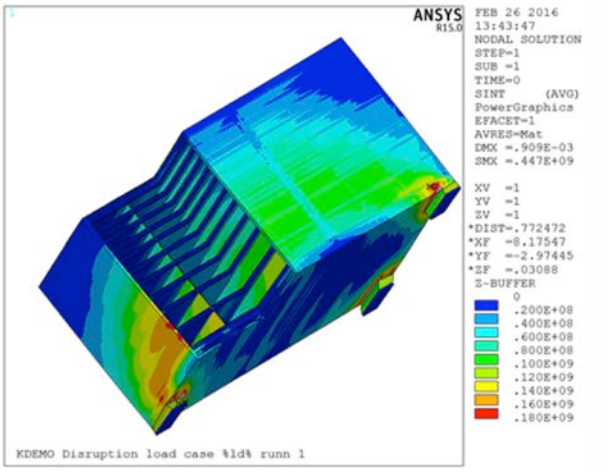

Figure 9. Disruption Eddy Currents Stresses on an outboard blanket module. The ANSYS model is cut away to show internal structure; attachments are represented by small rectangular features at corners.

The presence of higher permeability material increases the local field in the blankets and also increases the local change in field vs. time due to the disruption. The higher dB/dt induces more eddy currents which also cross with the higher local fields to produce higher loads. For inboard blankets in a high field tokamak, the saturation field of ~2T of the RAFM steel is significantly smaller than the main toroidal field component. For the K-DEMO situation, the static magnetic loading and the disruption eddy current loading are considered as separable with the provision that only including the induced eddy currents from a model with vacuum permeability may underestimate the disruption loading by amounts related to the magnetic steel fraction and the ratio of the saturation field to the toroidal field. The force will differ when the poloidal field is included. A uniform vertical field will not add to this but a field gradient will. So far the toroidal has dominated.

The radial static magnetic loads were applied to the blanket structural model. In this procedure the volume of the RAFM steel in the model is computed and the total load on the blanket is divided up equally among the nodes in the RAFM steel portion of the model. A peak stress of 55 MPa occurs near the support points (Figure 10), the contours have been adjusted to more clearly show the stress levels in the rest of the blanket structure. The stresses due to the static magnetic loading on the outboard blankets are small relative to thermal and the eddy current stresses, and this provides some justification for using the approximate method of quantifying the static magnetic loads.

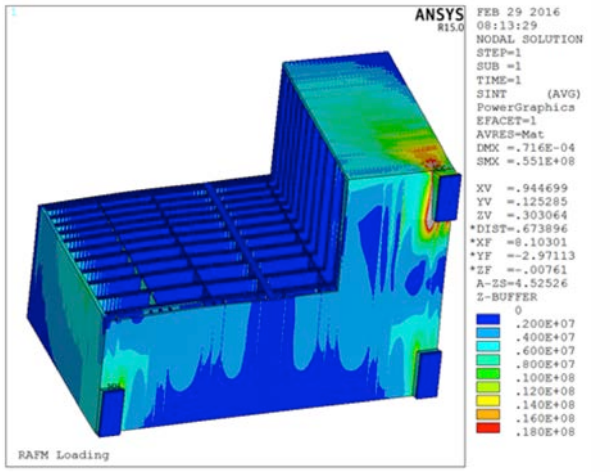

Figure 10. Stress due to static magnetic loading on a K-DEMO outer blanket module where the structural element are composed of RAFM steel.

3.4. Thermal Stress

Nuclear heat and radiation on the plasma facing surface of the blanket are the source of power input to the blanket. In steady state the coolant flows extract the input power. Nuclear heat and plasma surface heat fluxes are input to the model and a surface radiation of 0.4 MW/m^2 on

the tungsten first wall is assumed. Water in the cooling channels is held at a uniform temperature derived from NFRI analyses. A steady-state heat conduction analysis is performed which then gives a temperature distribution in the steel structure that is input to the thermal stress analysis. The temperature in the blanket structure is up to 566 °C. At 450 MPa, the calculated thermal stresses in the steel are the most significant of those investigated to date. The largest thermal stress occurs at the attachment points and in the ribs bridging across the breeding chambers.

4. Summary

Analyses needed to optimize the design of the K-DEMO facility have been carried out. Parameter scans for each of four different heating and current drive technologies have quantified the dependencies on key configuration variables, information needed to optimize the overall system. A concept for in-vessel systems compatible with large-sector maintenance and access for piping services has been proposed. Structural analyses focusing on the attachment of blanket modules to its support structure have quantified the stresses at the attachment points due to vertical displacement event-drive eddy-currents, to presence of magnetic material in the structure, and to thermal loading have been analyzed.

References

[1] KIM, K., et al., Nuclear Fusion **55** (2015) 053027.
[2] KIM, K., et al. Fusion Engineering and Design **88** (2013) 488–491.
[3] BIBET, P., et al., Nucl. Fusion, **35**, 1213, (1995)
[4] BECOULET, A., et al., Fusion Eng. Des., **86**, 490, (2011).
[5] IGNAT, D. W., et al, Nucl. Fusion **34**, 837, (1994).
[6] HARVEY, R. W., and MCCOY, M. G., 1993 Proc. Of the IAEA Technical Committee on Advances in Simulation and Modeling of Thermonuclear Plasmas (Montreal, Quebec) (Vienna: IAEA) pg 489. USDOC NTIS Doc. No. DE93002962.
[7] SMIRNOV, A., et al., in Proceedings of the 15th Workshop on ECE and ECRH, World Scientific, 2009, p. 301.
[8] BONOLI, P. T., et al, Proc. 21st International Conference on Fusion Energy (Chengdu, 2006) (Vienna:IAEA) CD-ROM file PD-3 and http://www-naweb.iaea.org/napc/physics/FEC/FEC2006/html/index.html.
[9] HEMSWORTH, R., et al, Nucl. Fusion **49**, 045006, (2009).
[10] GOLDSTON, R. J., et al, J. Comput. Phys. **43**, 61, (1981).
[11] PRATER, R., Physics of Plasmas **11** (2004) 2349–2376.
[12] LIN-LIU, Y.R., CHAN, V. S., and PRATER, R., Physics of Plasmas **10** (2003) 4064–4071.
[13] PRATER, R., et al., Nuclear Fusion **48** (2008) 035006.
[14] MARUSHCHENKO, N.B., et al., Physics of Plasmas **18** (2011) 032501.
[15] SMITH, G. R., et al., Physics of Fluids **30** (1987) 3633–3635.
[16] POLI, E., et al., Nuclear Fusion **55** (2015) 013023.
[17] FIGINI, L., et al., Plasma Physics and Controlled Fusion **57** (2015) 054015.
[18] GAROFALO, A., et al., Nuclear Fusion **54** (2014) 073015.
[19] WRIGHT, J.C., et al., Physics of Plasmas **11** (2004) 2473–2479.
[20] MESSIAEN, A., et al., Nuclear Fusion **50** (2010) 025026.
[21] PARK, J. S., *et al.,* Fusion Engineering and Design **100** (2015) 159–165